

5. SPRAY/WALL IMPINGEMENT

5.1 Wall Interaction Regimes

Wachters and Westerling (1966), Akao et al. (1980), Senda et al. (1994) and Nagaoka et al. (1994) describe in detail the phenomena observed when drops impinge on heated walls. The drop Weber number, $We_1 = \rho_l v^2 r / \sigma$, is an important parameter of the problem (v is the drop velocity component normal to the surface). At low approach velocities (low Weber numbers), drops rebound elastically from the wall. This is shown by the solid line in Fig. 5.1 which is a plot of the Weber number of the outgoing (rebounding) drop versus that of the incoming drop (Wachters and Westerling, 1966). With hot walls, a cushion of vapor fuel forms under the drop during the interaction preventing it from wetting the wall. As the approach velocity (Weber number) is increased, the normal velocity component of the rebounding drop decreases and the drop may actually break up into smaller drops. Beyond an incident Weber number of about 40 the liquid spreads out into a layer on the surface and the impinged liquid has little or no normal velocity component.

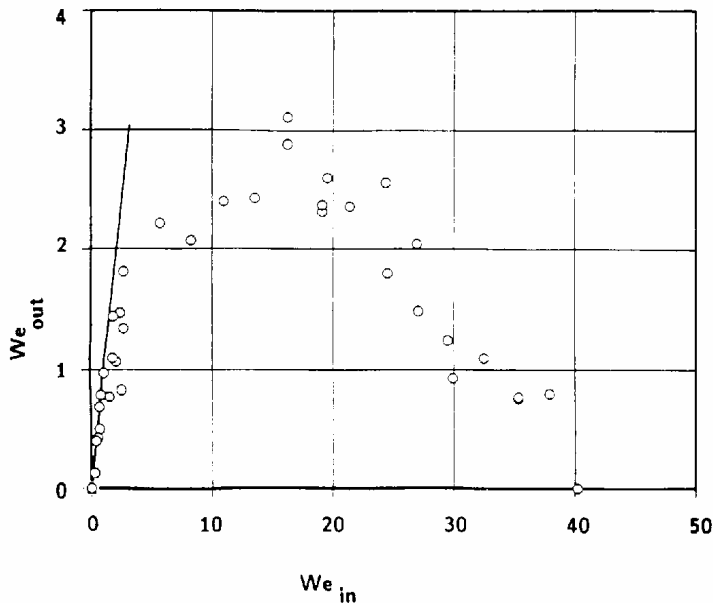


Fig. 5.1 Weber number of outgoing drop as a function of its approach Weber number for a wall collision (Wachters and Westerling, 1966).

Whether the wall liquid wets the surface or not depends on the wall temperature, wall material and roughness, approach angle of the incident drop and other factors (e.g., Wachters and Westerling, 1966, Yao and Cai, 1985). At high temperatures film boiling of the wall liquid takes place (Gottfried et al., 1966).

5.2 Wall Interaction Models

Three different drop-wall models were considered by Naber and Reitz (1988), as depicted in Fig. 5.2. In the first and simplest called Stick, drops that reach the wall stick to the wall at the impingement location and continue to vaporize. In the second model called Reflect, drops that reach the wall rebound with their tangential and normal velocity components unchanged, but the normal velocity component has opposite sign (specular reflection). In the third model called Jet, it is assumed that an incident drop leaves tangent to the surface in the manner of a liquid jet. The motivation for using this jet analogy can be seen by considering the limiting case of the impingement of a continuous stream of closely spaced drops, which would be expected to behave like a liquid jet.

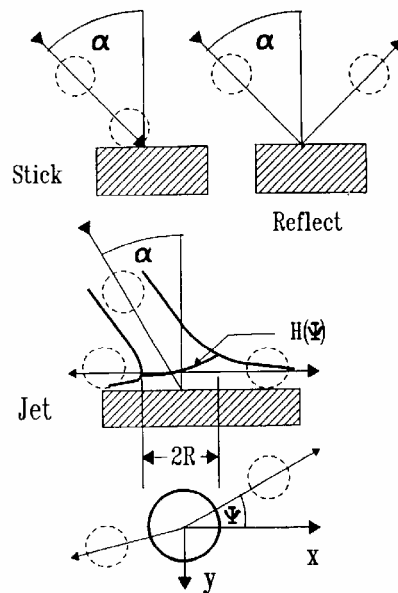


Fig. 5.2 Schematic diagrams of the Stick model (drops adhere to wall), Reflect model (drops rebound) and Jet model (drops glide along the wall) (Naber and Reitz, 1988).

Taylor (1966) considered the problem of a liquid jet impinging on an inclined wall. The jet is transformed into a sheet that flows outward along the wall. The problem can be solved analytically for a two-dimensional (planar) inviscid jet. In three dimensions (round jet) considerations of mass and momentum conservation alone (which are all that is needed in the 2-D case) are incapable of giving the angular distribution of thickness of the outgoing sheet, $H(\Psi)$ (see Fig. 5.2). Naber and Reitz (1988) introduced an empirical approach where the sheet thickness was assumed to be given by

$$H(\psi) = H_{\pi} \exp(\beta(1 - \psi / \pi)) \quad (5.1)$$

where H_{π} is the sheet thickness at $\Psi=\pi$ and β is a parameter determined from mass and momentum conservation, i.e.,

$$\rho_l q \pi a^2 = 2 \int_0^{\pi} \rho_l q R H(\psi) d\psi \quad (5.2)$$

$$\rho_l q^2 \pi a^2 \sin \alpha = 2 \int_0^{\pi} \rho_l q^2 R H(\psi) \cos \psi d\psi \quad (5.3)$$

where α is the jet inclination angle, 'a' is the radius of the approaching jet and R is the radius of the circle at which the sheet thickness, $H(\Psi)$ is defined (see Fig. 5.2). The fluid which flows out between Ψ and $\Psi+d\Psi$ is proportional to the sheet thickness since in potential flow the liquid velocity (speed), q, does not change along streamlines. Combining Eqs. (5.2) and (5.3) gives

$$\sin \alpha \int_0^{\pi} H(\psi) d\psi = \int_0^{\pi} H(\psi) \cos \psi d\psi$$

or, with Eq. (5.1)

$$\sin \alpha = \left(\frac{\exp(\beta) + 1}{\exp(\beta) - 1} \right) / 1 + (\pi / \beta)^2 \quad (5.4)$$

which is the expression for β .

It was further assumed that the angle, Ψ , at which an impinging drop leaves the surface can also be found from the liquid jet analysis. In this case the

function $H(\Psi)$ is interpreted as the probability that a drop leaves in a direction between Ψ and $d\Psi$, and the angle is obtained by integrating Eq. (5.1) as

$$\psi = -\frac{\pi}{\beta} \ln\{1 - p(1 - \exp(-\beta))\} \quad (5.5)$$

where p is a random number uniform on the interval (0,1). This assumption is consistent with the stochastic method of solution of the spray equations used by Naber and Reitz (1988).

Naber and Reitz (1988) tested the models with experimental data on the impingement of sprays on inclined flat plates by Kuniyoshi et al. (1980), and with an endoscope study of sprays on a piston bowl wall by Werlberger and Cartellieri (1987). They concluded that the Jet model agreed best with the data.

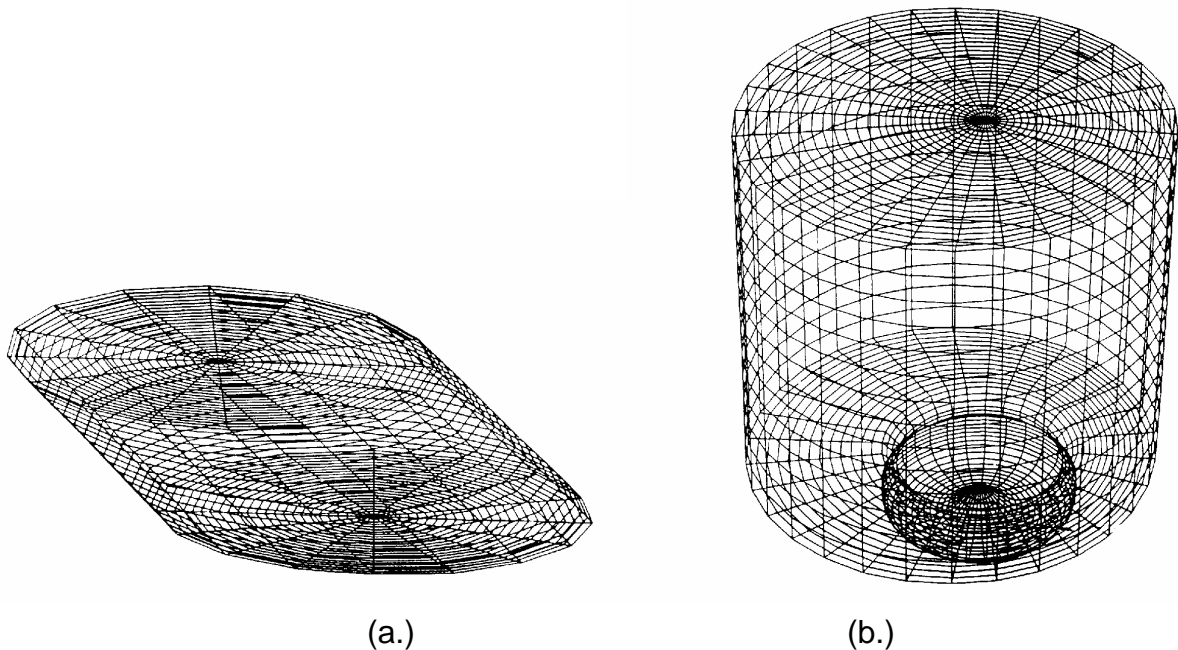


Fig. 5.3 Computational domains for a.) inclined flat plate study, b.) direct injection engine used by Naber and Reitz (1988).

The computational meshes used in their study are shown in Fig. 5.3. Figure 5.3a shows a mesh used in the inclined flat plate study for the 45 degree inclination case. The domain was an inclined cylinder with radius 60 mm and length along the cylinder axis of 63 mm. The mesh spacing was nonuniform with finer axial resolution close to the top and bottom faces of the cylinder. The injector was

located at the pole of the mesh on the top face of the cylinder, and the injector orifice diameter was 0.29 mm.

Figure 5.3b shows a three-dimensional view of the computational mesh used for the engine study. The engine was an AVL 0.5-L high-speed direct-injection single-cylinder research diesel engine (Type 528). The engine's speed was 1800 rev/min and the bore and stroke were 85 mm and 92 mm, respectively. The fuel nozzle had two 0.21 mm diameter holes and the injector was located on the head (top face of the domain) at the pole of the mesh directly above the cusp in the piston bowl. The diesel fuel used in both sets of experiments was modeled using tetradecane

Figure 5.4 shows computed details of spray structure 5.3 ms after the beginning of injection for a wall inclination of 26.6 degrees (gas pressure 6.28 MPa, injection pressure 37.3 MPa). The gas velocity field (Fig. 5.4a) reveals a wall-jet emanating radially outward from the spray impingement site. The head of the jet contains a vortex that is largest at the forward edge of the jet (i.e., along the line of projection of the incoming spray on the wall). The vortex is smaller at the rear of the wall jet. The computations showed that the strength of the rear vortex decreased as the wall inclination angle was increased.

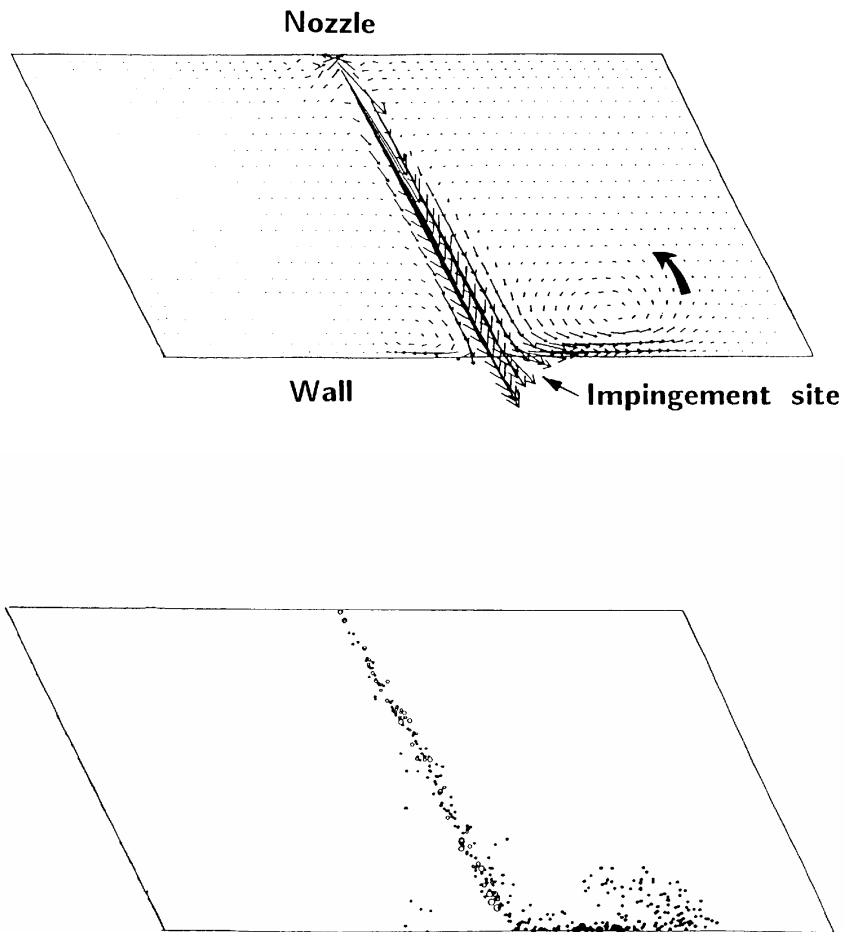


Fig. 5.4 Computed spray structure in the spray symmetry plane. a.) gas velocity vectors, b.) drop parcel locations showing wall-jet vortex (Naber and Reitz, 1988).

Figure 5.4b shows the spray parcels in the spray symmetry plane. The small drops can be seen to be deflected away from the wall by the gas wall-jet flow, forming a wall spray. These drops are entrained in the gas wall-jet vortex. Larger drops with correspondingly higher momentum impinge on the wall and then move along the wall.

There is little interaction between the spray and the wall at high impingement angles, as shown in Fig. 5.5, which compares predicted and measured spray outlines at different wall impingement angles. For large values of α the entire spray is deflected away from the wall. The agreement between the computed and measured spray outlines is reasonably good. However, the computed spray generally underestimates the measured spray outlines. This could be because photographs of sprays are most sensitive to the smallest drops (which scatter light efficiently) and the computations consider only a limited range of drop size.

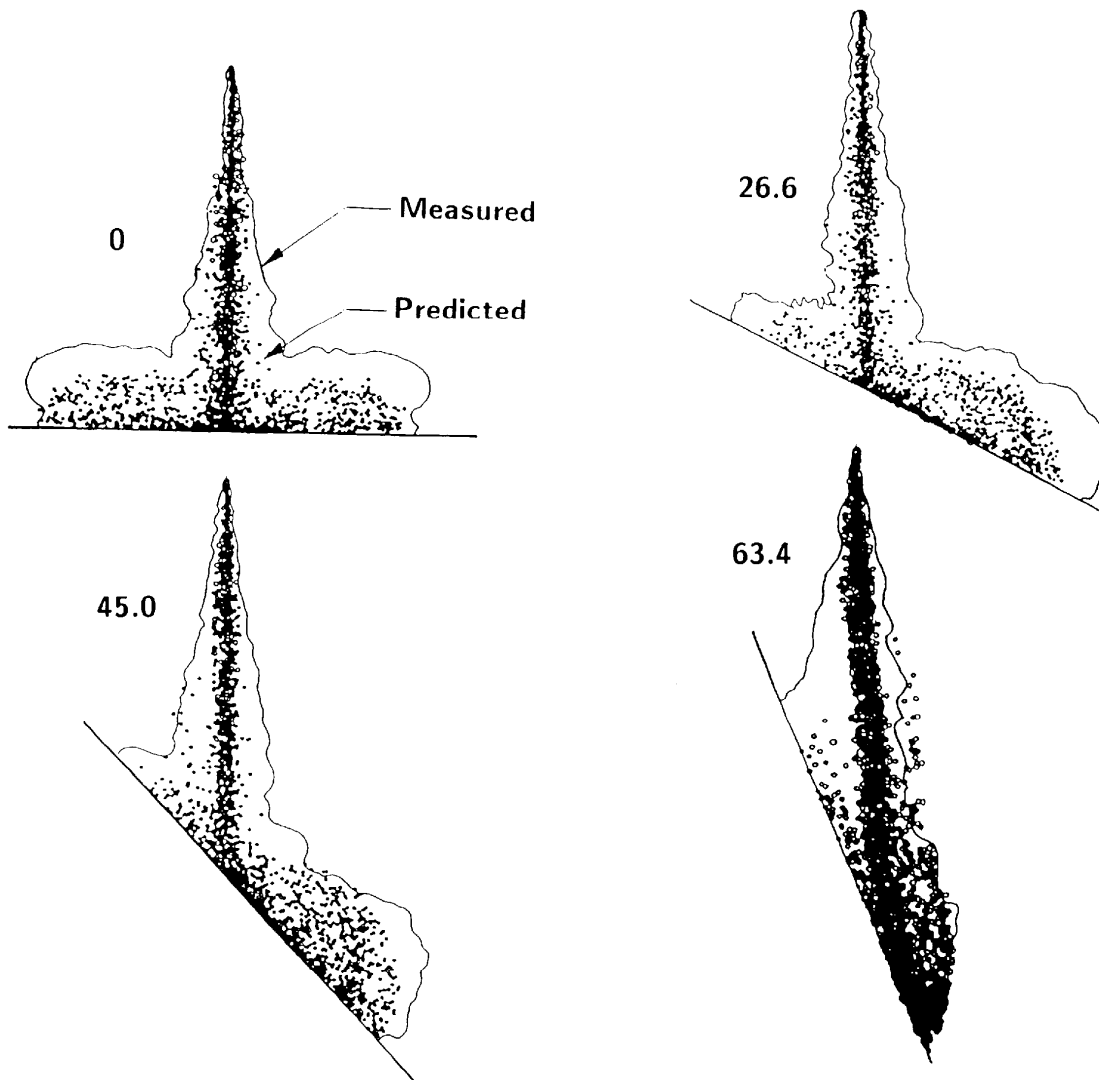


Fig. 5.5 Comparison of predicted spray parcel locations with the photographic spray outlines of Kuniyoshi et al. (1980) for inclination angles of 0, 26.6, 45 and 63.4 degrees (Naber and Reitz, 1988).

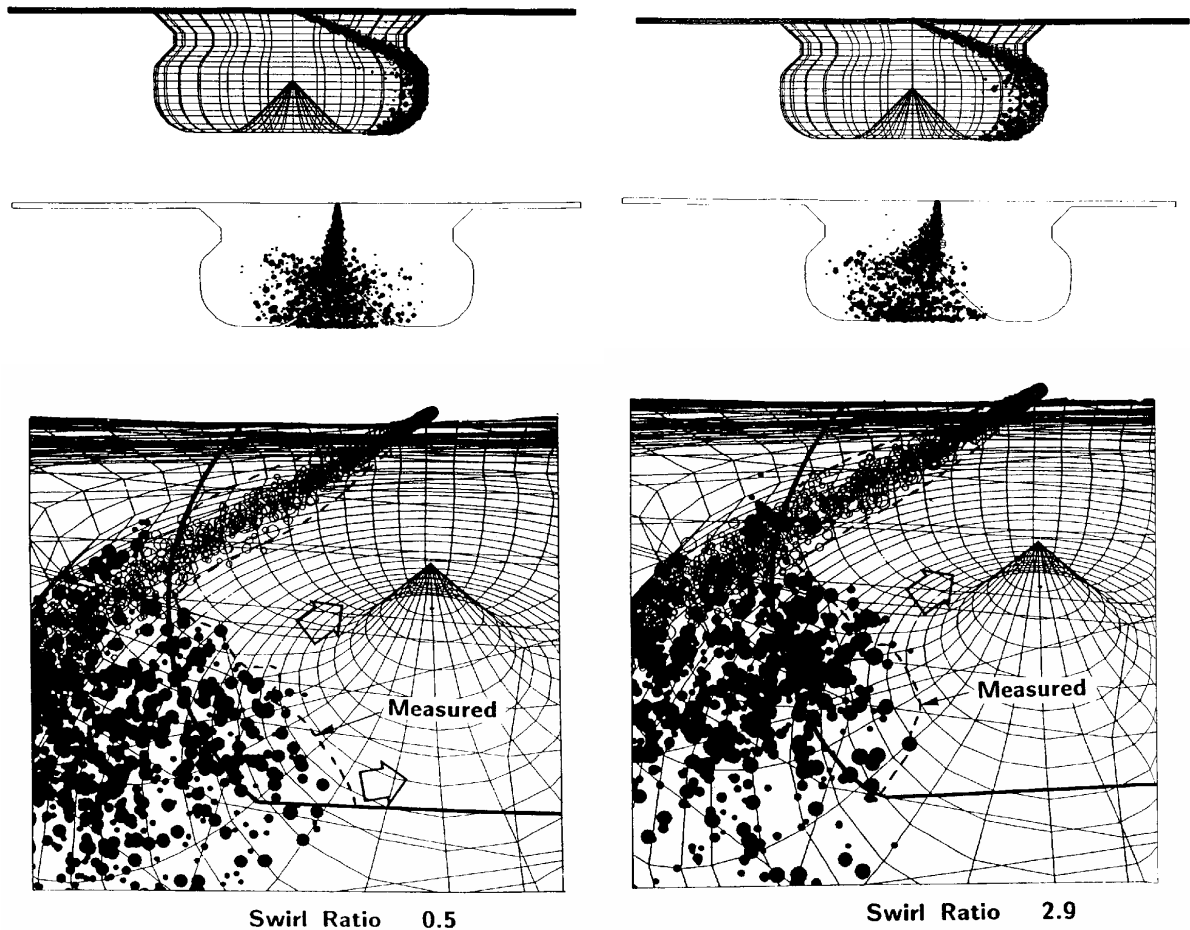


Fig. 5.6 Wall impingement details at TDC in the AVL engine predicted by Naber and Reitz (1988) using the Jet model. Left- low swirl, right - high swirl. Top - elevation views, bottom - perspective view. Dashed lines - spray outline from endoscope study of Werlberger and Cartellieri (1987).

Figure 5.6 shows results obtained by Naber and Reitz (1988) for the low and high swirl cases of the engine study at TDC (top-dead-center) (swirl ratio 0.5 and 2.9, respectively). In the perspective view, the field of view is the same as that seen by the endoscope system of Werlberger and Cartellieri (1987). The injector tip is located near the right-hand top of the diagrams, and the spray is directed toward the left, downward into the bowl. The cusp in the center of the piston bowl is located directly below the nozzle. The endoscope was in the head at the edge of the bowl looking down into the bowl and the experimental field of view is indicated by the heavy solid lines. The dashed lines show the visible spray outlines seen in the endoscope pictures. It can be seen that the actual

spray impingement point on the piston bowl wall (middle left-hand edge of Figs. 5.5) was slightly outside the field of view of the endoscope.

The extent of spread of the experimental and predicted wall sprays can be seen to agree well in Fig. 5.6 for both low and high swirl cases. The spray/wall interaction creates a liquid layer that stays close to the piston bowl wall and extends down to the floor of the piston bowl. The spray is deflected by the swirl in the high swirl case.

In the flat plate results, drops that hit the wall were obscured from view by the surrounding smaller spray drops that never contacted the wall because they were deflected away by the gas wall-jet. In the engine these small drops vaporize and disappear in the hot chamber gas, and this reveals the liquid that has contacted the wall.

The Naber and Reitz (1988) spray/wall interaction model has been improved by Gonzalez et al. (1991) who noted that in cold-starting diesel engine applications the impinging drop Weber number can be less than 40 since drop velocities are low and drop sizes are large due to the high fuel viscosity at low temperatures. Gonzalez et al. (1991) curve-fitted Wachters and Westerling's (1966) results shown in Fig. 5.1 with the correlation

$$We_o = 0.678We_i \exp(-0.088We_i) \quad (\text{for } We_i < 40) \quad (5.6)$$

(the subscripts 'o' and 'i' refer to the outgoing and incoming drop respectively). Equation 5.6 was used to compute the normal velocity of drop rebound Weber numbers less than 40. At higher We_i , the Jet model of Naber and Reitz (1988) was used. Note that in this model there is no frictional resistance between the impinged drops and the wall and the drops (i.e., liquid 'blobs') continue to interact with the gas as they move along the wall.

5.3 Wall Atomization

Naber and Reitz (1988) and Gonzalez et al. (1991) assumed that the drop's diameter does not change during the wall interaction in both the drop rebound and slide regimes. In reality, impinging drops at high Weber numbers disintegrate following the wall interaction. Takeuchi et al. (1982) experimentally identified six possible modes of breakup when a drop impinged on a hot surface at atmospheric pressure including modes: where the drop rebounds from the surface with or without subsequent atomization; where vapor bubbles from the hot surface blow through the liquid film on the surface causing breakup; and where the drops do not contact the surface due to the presence of a thin vapor film.

The breakup of drops that impact the wall was considered by Eckhause and Reitz (1994) who modeled enhanced secondary breakup of drops that impinge on the wall surface by setting the breakup time model constant as $B_1=1.73$ for those drops that impinge on a wall, consistent with the results of Liu et al. (1993) for drops that are suddenly exposed to a violent disturbance. The computations were performed using KIVA with the 2-D axisymmetric domain shown in Fig. 5.7, and comparisons were made with the experimental data of Naber et al. (1988). In the experiments, high pressure sprays impinged on a raised pedestal within the piston bowl under conditions similar to those at TDC in a diesel engine.

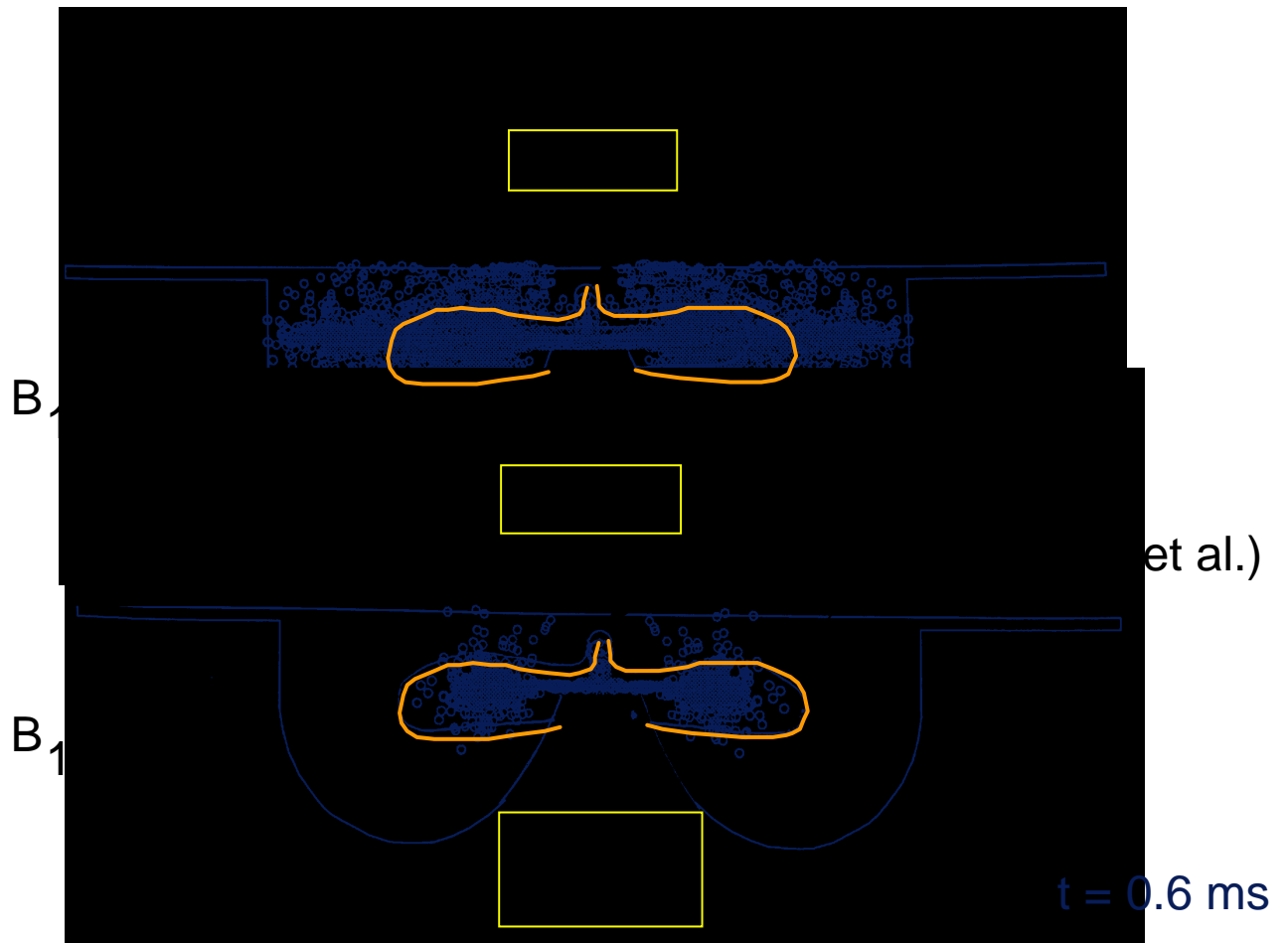


Fig. 5.7 Predicted and measured spray penetration, 0.6 ms after the beginning of injection using two different values of the breakup model time constant, B_1 in Eq. (3.15) (Eckhause and Reitz, 1994).

As can be seen, the predicted spray penetration after impingement depends strongly on the value of the breakup model constant, B_1 . In particular, good agreement with the experimentally measured spray penetration is obtained when the value $B_1 = 1.73$ is used. This suggests that drops that suddenly impact a solid surface, or drops that are suddenly exposed to a high velocity air stream (as in the experiments of Liu et al., 1992) are destabilized, and that this destabilization process can be accounted for by using a smaller value of the breakup time constant, B_1 . Alternative breakup models have been proposed by Senda et al. (1994).

5.4 Wall Heat Transfer

The formation of a continuous liquid film that wets the wall is also not described by the Naber and Reitz (1988) wall interaction model. Liquid film details influence heat transfer and vaporization rates in high temperature applications. Naber and Farrell (1991) studied drop impingement under diesel engine conditions where the combustion chamber pressures are greater than the critical pressure of the impinging fuel. They observed that for surface temperatures below the critical temperature, wall-wetting occurs even at supercritical pressures. For surface temperatures above the critical temperature a non-wetting (Leidenfrost) regime was present. They then concluded that for diesel engines, where the normal in-cylinder surface temperature ranges from 400 - 600 K, the appropriate hydrodynamic regime is the wetting regime.

This observation was used by Eckhause and Reitz (1995) to formulate a spray/wall heat transfer model in the KIVA code. The model does not account for Leidenfrost effects, but it does consider flooded and non-flooded regimes depending on whether or not a liquid film is determined to be present on the surface, respectively. In the flooded case heat transfer is modeled based on boundary layer correlations. In the non-flooded regime heat transfer is modeled by considering correlations for individual drops impinging on a surface.

The total heat transfer from the surface to a drop or film is found from

$$Q = hA(T - T_s)t_{res} + Q_g \quad (5.7)$$

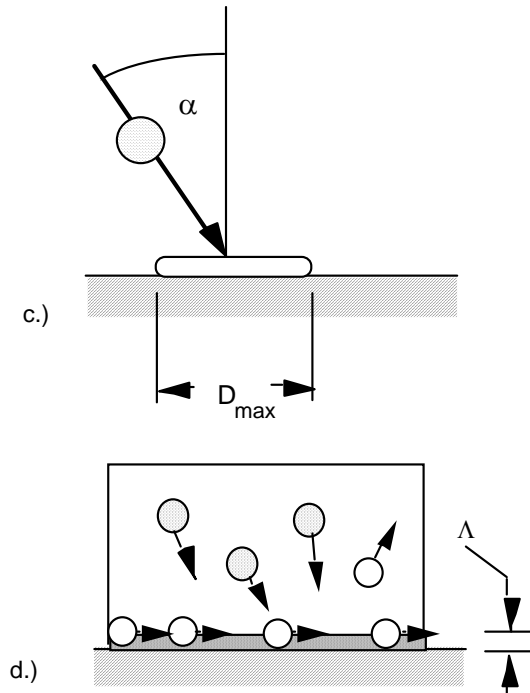


Fig. 5.8 a.) Drop spreading on impact. b.) representation liquid film formation of thickness Δ in a computational cell. The film is the collection of impinged drops with $We_i > 40$.

where A is the liquid area in contact with the wall, $h = Nu K/\Delta$ is the convective heat transfer coefficient, Nu is the Nusselt number, Δ is equal to the drop diameter, d , or, for flooded cases, to the film thickness Δ . K is the liquid thermal conductivity, T is the liquid drop or film temperature, T_s is the surface temperature, t_{res} is the residence time for the liquid on the surface and Q_g is the heat transfer from the gas (only relevant when a film is present).

Wachters and Westerling's (1966) criteria were used as described by Gonzalez et al. (1991), and a drop with an incoming Weber number greater than 40 was assumed to slide along the surface for heat transfer purposes, following the Jet impingement model of Naber and Reitz (1988). A drop with an incoming Weber number less than 40 was assumed to rebound from the surface after a residence time in contact with the surface equal to the first order vibration period of the drop

$$\tau = (\pi / 4) \sqrt{\rho d^3 / \sigma} \quad (5.8)$$

during which heat is transferred to the drop.

Drops with Weber numbers less than 40 do not contribute to a film since they rebound from the surface or film. Eckhause and Reitz (1994) computed the film thickness, Δ , (see Fig. 5.8) by taking the total mass of drops whose impingement Weber number was greater than 40, and dividing by the fuel density, and the surface area of the cell. The film temperature was the mass average temperature of all film drops. For an impinging drop that slides along the surface, whether or not that drop is part of a film, the residence time is the time it stays in contact with the wall, and the area of contact with the surface in the flooded regime is surface area of the flooded cell. However, for an individual impinging drop the average contact area, $A = \pi (D_{\max}/4)^2$, is based on the spreading equation of Akao et al. (1980), where the drop spreading diameter $D_{\max} = 0.613 d We_i^{0.39}$ (see Fig. 5.8).

The gas phase heat transfer was found using the modified law-of-the wall described by Reitz (1991). The liquid phase heat transfer in the flooded regime was based on heat transfer correlations for boundary layer flow of the form $Nu = 3.32 Pr^{1/3}$. For the non-flooded regime, the Nusselt number for individual drop evaporation was assumed to be 2.0. To compute the temperature change of a drop or film in contact with the wall, an energy balance is performed of the form

$$\Delta T = Q / m C_f \quad (5.9)$$

where C_f is the specific heat of the fuel, and m is the film or drop mass. In the flooded regime this computation is performed on an individual cell basis, and in the non-flooded and rebounding cases it is done for each individual drop.

The performance of the model has been assessed by comparisons with experimental data. Wolf and Cheng (1989) used a rapid compression machine with an end-of-compression temperature of 897 K and a wall temperature of 343 K. Heat flux was measured at the impingement point for sprays injected at various distances from the wall. The injector nozzle exit diameter was 0.254 mm and the injection duration was 4.3 ms.

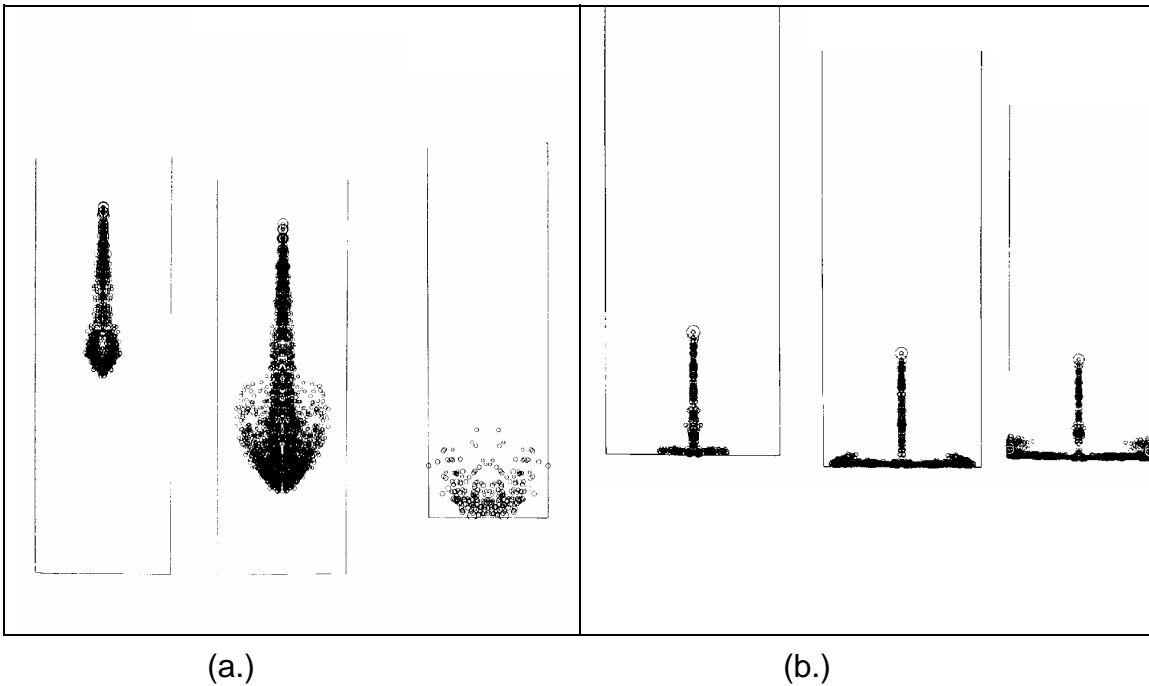


Fig. 5.9 Predicted sprays for impingement distance of a.) 105 mm at 4 ms and b.) 29 mm at 1 ms intervals (Eckhause and Reitz, 1994)

The predicted spray breakup pattern for an impingement distance of 105 mm is shown in Fig. 5.9a. The spray breaks up and is mostly vaporized by the time it impinges at about 8 ms after injection. The predicted heat flux due combined gas and liquid phase heat transfer is shown in Fig. 5.10, and is in reasonable agreement with the experimental results of Wolf and Cheng (1989), but the computed heat flux is larger than that measured at the end of the comparison period. This could be due to uncertainties in the injection velocity which was assumed to be constant in the simulations while in the experiments the injection pressure varied with time. The liquid phase heat transfer at 8 ms after injection contributes a small hump to the heat transfer curve which is also seen in the experiments.

The spray breakup pattern for the 29 mm impingement distance is shown in Fig. 5.9b. There is little breakup before impingement at such a close distance. The spray impinges and spreads out along the wall (and even up the end walls of the computational domain).

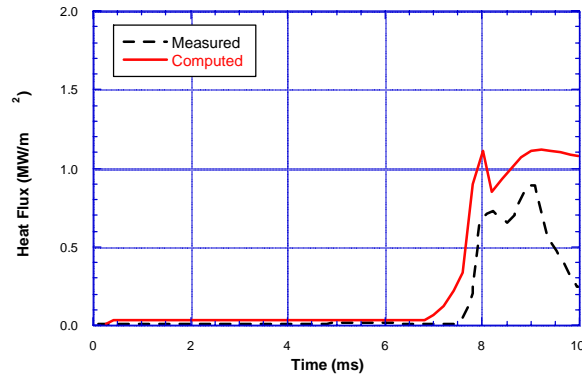


Fig. 5.10 Wall heat transfer predictions compared to experimental data for 105 mm impingement distance (Eckhause and Reitz, 1994).

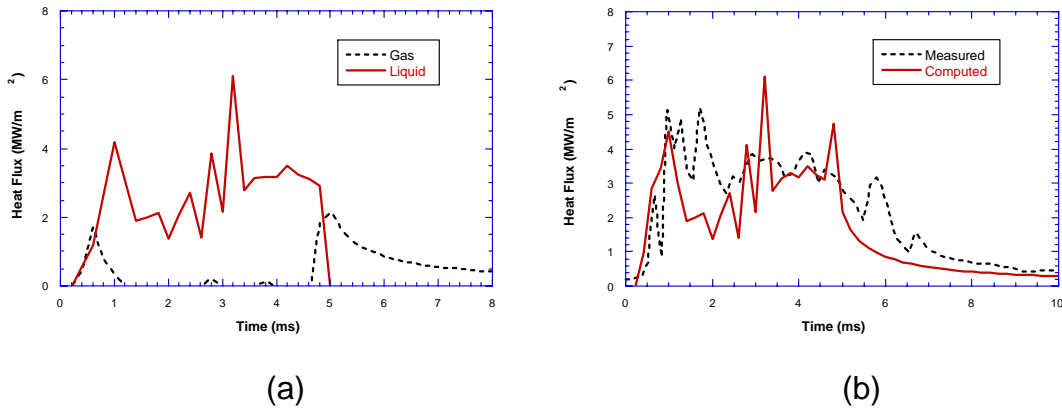


Fig. 5.11 Wall heat transfer contributions from (a.) the gas and the liquid phase and (b.) the combined gas and liquid wall heat transfer together with experimental data for 29 mm impingement distance.

The predicted heat transfer results are shown in Figs. 5.11a and b. The gas phase heat transfer exhibits a lull where a film is present on the surface from 1 ms to 5 ms after injection (Fig. 5.11a). The combined liquid and gas phase heat transfer is in reasonably good agreement with the experiment heat flux measured as can be seen in Fig. 5.11b. The liquid phase heat transfer peaks near the beginning and end of impingement (because the film is the thinnest at these points), but a peak is also located in the middle of the flooded phase - probably due to a brief thinning of the film.